A&A 396, 581–587 (2002)
DOI: 10.1051/0004-6361:20021272

Astronomy & Astrophysics

Imaging the circumstellar envelope of OH 26.5+0.6

D. Fong[1], K. Justtanont[2], M. Meixner[1], and M. T. Campbell[1]

[1] Department of Astronomy, University of Illinois, 1002 W. Green Street Urbana, IL 61801, USA
[2] SCFAB, Stockholm Observatory, Department of Astronomy, 106 91 Stockholm, Sweden

Received 10 July 2002 / Accepted 28 August 2002

Abstract. Using the Berkeley-Illinois-Maryland-Association (BIMA) Millimeter Array, we were able to map the extreme OH/IR star, OH 26.5+0.6, in the ^{12}CO $J = 1$–0 line transition. The CO emission is partially resolved with a deconvolved source size of $8.5'' \times 5.5''$. The spectrum shows that the blue-shifted emission is missing, most likely due to interstellar absorption. By modelling the infrared spectral energy distribution, we derive a dust mass loss rate of 1.9×10^{-6} $M_\odot$ yr^{-1}. From this we are able to place an upper limit on the extent of the dusty envelope of 10^{16} cm while our BIMA map shows that the CO photodissociation radius extends out to about 7×10^{16} cm. To best fit the BIMA observations and the higher CO rotational transitions using our full radiative transfer code, we needed to include a second, more tenuous AGB wind, outside the high density superwind to account for the observed flux. From our model, we conclude that up to 80% of the CO flux comes from the unresolved superwind.

Key words. stars: AGB and post-AGB – stars: circumstellar matter – stars: individual : OH 26.5+0.6 – stars: late-type – stars: mass loss

1. Introduction

A star loses a significant fraction of its initial mass when it evolves up the Asymptotic Giant Branch (AGB). During this phase, mass loss drives the evolution of the star. It is thought that mass loss increases dramatically towards the tip of the AGB in what is called a superwind (Iben & Renzini 1985) that ejects most of the remaining envelope of the star. There is ample observational evidence to support this hypothesis, e.g., axisymmetric proto-planetary nebulae supposedly created by an equatorially enhanced superwind (Ueta et al. 2000), as well as a fast bipolar flow into a denser AGB wind (Bujarrabal et al. 2002), core-halo structures seen in CO observations of evolved stars suggesting the presence of dual winds, particularly AFGL 618 (Meixner et al. 1998), concentric shells of enhanced mass loss around AFGL 2688 (Sahai et al. 1998) and partial shells seen around the C-rich star, IRC+10216 (Mauron & Huggins 1999). The superwind enhanced mass loss is on the order of a factor of ten or more higher than the AGB mass loss which occurs during most of the star's AGB lifetime.

Some extreme OH/IR stars have been observed to have low CO $J = 1$–0 and $J = 2$–1 emission (Heske et al. 1990). This is contrary to the observed infrared spectral energy distribution. The 10 μm silicate of these stars are in absorption, indicating a large dust column density and hence a very high dust mass loss rate. It was suggested that these stars have recently undergone the superwind phase. One such star is OH 26.5+0.6. It is a strong OH maser emitter (e.g., te Lintel Hekkert et al. 1989) with a wind terminal velocity of 15 km s^{-1}. Bowers & Johnston (1990) mapped the OH maser around the star and found the full shell radius of about 4″. The estimated distance to the star is 1.4 kpc from phase lag techniques (van Langevelde et al. 1990). Meyer et al. (1998) reported a detection of water-ice in the circumstellar envelope which indicates that the mass loss rate is high enough to shield water molecules. Justtanont et al. (1996) modelled the star in both the IR and CO up to $J = 4$–3 and confirmed the presence of a superwind. OH 26.5+0.6 was observed with the IRAM 30 m and IRAM interferometer at Plateau de Bure (Neri et al. 1998), but the ^{12}CO $J = 1$–0 line was contaminated due to galactic confusion. In this follow up paper to Justtanont et al. (1996), we report the first detection and maps of ^{12}CO $J = 1$–0 around OH 26.5+0.6, along with detailed models of the circumstellar envelope.

2. Observations

Interferometric observations of OH 26.5+0.6 were made with the Berkeley-Illinois-Maryland-Association (BIMA) Millimeter Array from May to November 1999. The instrument is described in detail by Welch et al. (1996). We observed the ^{12}CO $J = 1$–0 line transition, at 115.2712 GHz, with the BIMA 10 element array in three configurations: B, C and D. However, only C and D array data, with projected baselines spanning 2.4–34 kλ, were included in the final maps because of poor observing conditions during the B array observations. The OH 26.5+0.6 observations were interleaved every 27 min with the nearby point source, 1733-130, to track the phase variations over time. The absolute flux calibration

---

Send offprint requests to: K. Justtanont, e-mail: `kay@astro.su.se`

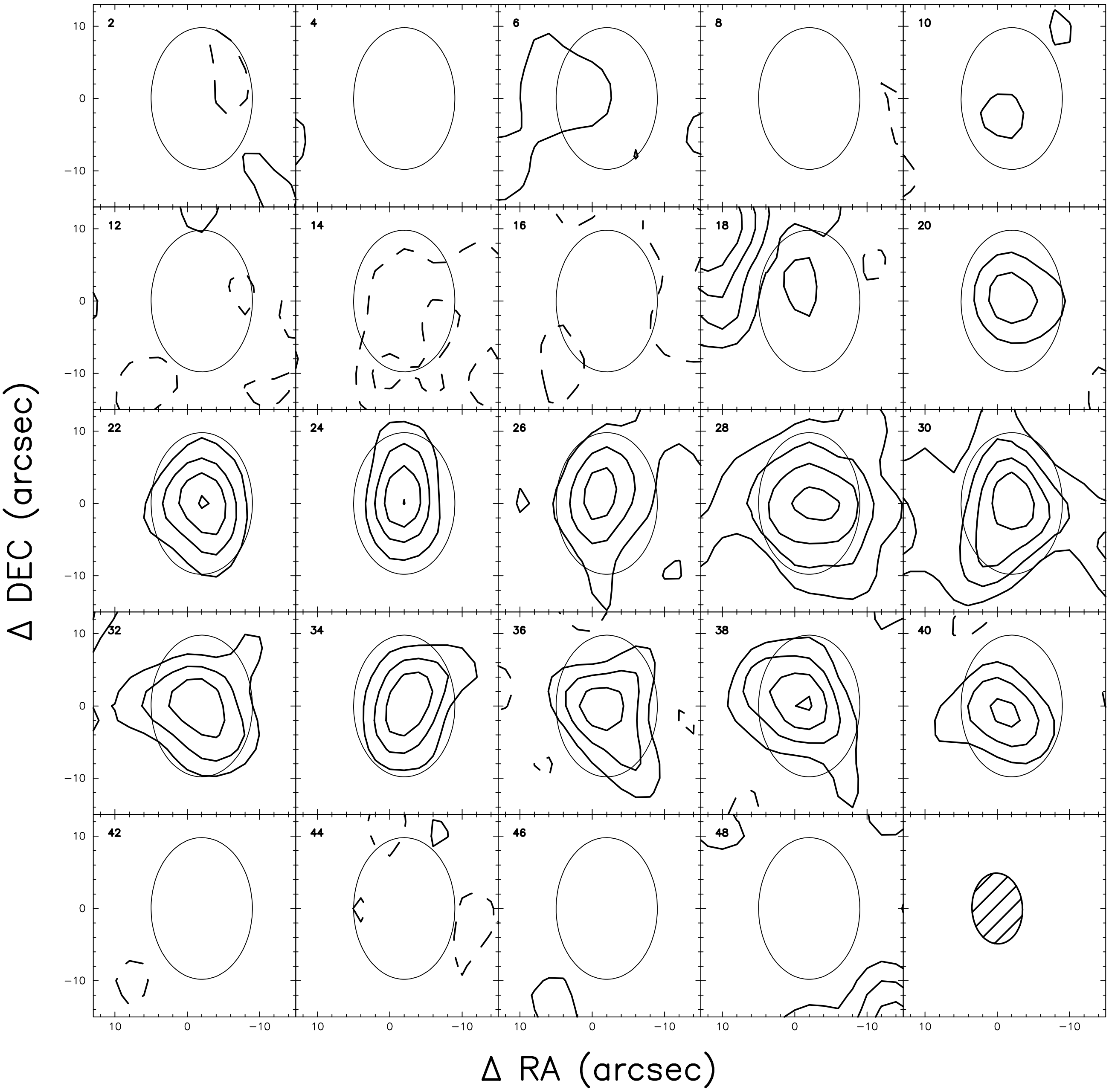

Fig. 1. Velocity channel maps of OH 26.5+0.6. The contour levels are in increments of 2σ. The first detectable CO emission is at 18 km s^{-1}. The beam is shown on the bottom right panel. The ellipse in each channel is twice the beam size and outlines the mask region.

was determined from observations of Neptune and is accurate to within 20%. The final maps have an accumulated on source observing time of 13 h.

Typical single sideband system temperatures ranged from 500–1200 K. The observed correlator mode covered a bandwidth of 50 MHz, resulting in a velocity coverage of 128 km s^{-1} with a resolution of 1 km s^{-1}. The phase center of the map was α(J2000) 18h37m32.52s, δ(J2000) $-5°23'59.39''$. Data reduction was performed in the MIRIAD software package (Sault et al. 1995). Standard data reduction, calibration, imaging and deconvolution procedures were followed. The data were self-calibrated to remove the residual phase errors. Robust weighting of the visibility data gave a $9.8'' \times 7''$ CLEAN beam with a position angle of 2.4°. The typical rms noise per 2 km s^{-1} channel is 0.14 Jy Beam^{-1}.

3. Results

^{12}CO $J = 1$–0 was detected and imaged for the first time around OH 26.5+0.6. The velocity channel maps (Fig. 1) have velocity widths of 2 km s^{-1} and the contour levels are in increments of 2σ. The circumstellar CO emission is first seen at 18 km s^{-1} and ends at 41 km s^{-1}. The morphology and kinematics of the molecular gas is roughly consistent with a spherically expanding envelope, where the systemic velocity component contains the most extended emission, while the increasingly blue- and red-shifted velocities decreases in spatial extent until the most compact emission is seen at the extreme velocity tips situated at the center of the source. The systemic velocity component appears to lie between 27–30 km s^{-1} which is consistent with the higher CO transitions

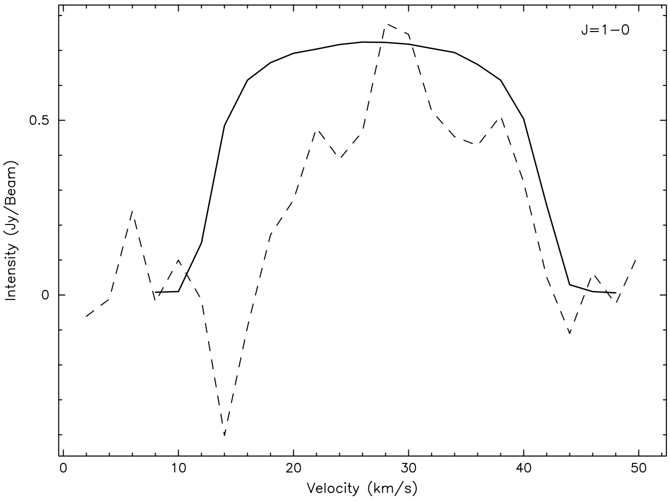

Fig. 2. The CO line profile of the emission within the masked region (dashed line). Notice the missing flux at the blue-shifted edge of the profile. The solid line is the model prediction (see Sect. 4).

(Justtanont et al. 1996) and OH maser observations (Bowers & Johnston 1990).

Interferometric observations are better suited to observe compact galactic plane sources than single dish telescopes because arrays achieve much higher angular resolutions which help to isolate the source within confused regions. Furthermore, an interferometer inherently acts to spatially filter out the more extended emission. Even with these advantages we still had difficulties discriminating the source emission from intervening interstellar clouds.

The most blue-shifted circumstellar emission is seen at 18 km s^{-1}. Although it is only detected at the 2 σ level, we believe that it is real because the clump is located at the phase center and appears to be an extension of the velocity structure from the subsequent velocity channel. The bright emission found at the NE quadrant of this channel map is interstellar cloud contamination. On the contrary, we do not believe the 2σ signal at the 10 km s^{-1} channel is associated with the circumstellar envelope of OH 26.5+0.6 since both the OH maser maps (Bowers & Johnston 1990) and CO line profiles of higher transitions (Justtanont et al. 1996) do not extend to this low velocity. Intervening interstellar emission is also found from 26–32 km s^{-1}. Since the contamination overlaps with the source emission, the structure of the circumstellar envelope is not accurately represented in those channel maps. For example, at 28 km s^{-1}, the emission is too extended. For a spherically expanding envelope, the emission at the systemic velocity is expected to have the greatest spatial extent, but there should be a gradual increase in the size from the compact emission seen at the extreme blue- and red-shifted velocities to the systemic velocity. However, the observations show a sudden expansion in size at 28 km s^{-1} and intervening emission is seen merging in at the periphery. This would suggest that the more extended emission is not associated with the source. Subtle hints of interstellar contamination between 26–32 km s^{-1} is also seen in the higher CO transitions.

Our procedure to separate out the interstellar cloud contamination from the source is simply to mask out all the emission outside twice the beam area. The ellipse shown on the channel maps outlines the mask region. The line profile of the emission within the mask region is shown in Fig. 2. Without applying the mask, the profile will spuriously spike up at velocities containing interstellar contamination. The emission peak between 28–30 km s^{-1} is partially due to the presence of interstellar contamination found within the mask region. The absorption feature seen at 14 km s^{-1} is most likely an interferometer artifact. This is caused by the missing short spacing information that all interferometers suffer. For BIMA, extended emission that has spatial scales larger than ~40″ will be increasingly resolved out (Helfer et al. 2002). Hence the resulting map will contain a bowl of negative surface brightness. In contrast, single dish telescopes have detected bright and extended galactic background emission at 14 km s^{-1} in the higher CO transitions (Heske et al. 1990; Justtanont et al. 1996). Since OH 26.5+0.6 is much smaller than 40″, BIMA will detect all the flux for this compact object.

The ^{12}CO $J = 3$–2 and 4–3 lines (Justtanont et al. 1996) show that the circumstellar expansion ranges from 11–42 km s^{-1}. The blue-shifted $J = 1$–0 line emission, however, only goes out to 18 km s^{-1}. Similarly, the $J = 2$–1 velocity profile (Heske et al. 1990) is also missing blue-shifted emission ranging from 11–17 km s^{-1}. Their procedure to correct for the strong interstellar contamination, by subtracting emission from a nearby position, may have been responsible for the missing wing. However, no subtraction was performed on the BIMA $J = 1$–0 observations and still the line profile exhibits this missing blue-shifted wing. OH maser maps clearly indicate that the circumstellar expansion ranges from 11 to 42 km s^{-1} (Bowers & Johnston 1990), consistent with the ^{12}CO $J = 3$–2 and 4–3 lines. From HI galactic gas studies, foreground gas participating in galactic rotation is expected to range from about 0 to 20 km s^{-1} (Burton 1988). Galactic HI is roughly coincident with the galactic CO clouds since HI is expected to be found near the photodissociated interface of the molecular clouds (see e.g., Hollenbach & Tielens 1997). Thus the cold foreground CO gas is most likely responsible for the blue-shifted line absorption found in the the lower CO transitions.

There are clear differences between the spatial distribution of the CO and OH maser emission. Our CO maps are partially resolved with an average *FWHM* extent of 13″ × 8.9″. The average envelope size is obtained by fitting an elliptical gaussian to the channel maps, excluding the contaminated images and the edge channels. The deconvolved source size is 8.5″ × 5.5″ (*FWHM*). The well resolved OH images show a complete spherical shell (1–2″ in width) with clumpy structures and a full spatial extent of ~8″. OH maser emission is found around the star where the velocity, density and UV conditions are optimal for masers to occur. The maser regions do not necessarily trace the mass (Bowers & Johnston 1990). In contrast, CO is the best tracer of the nebular mass. The BIMA images show that CO is concentrated in the core and becomes diffuse farther out in radius (see Sect. 4 for more discussion).

Table 1. Input parameters for models of the dust and gas envelopes of OH 26.5+0.6.

Stellar mass	8 $M_\odot$
Stellar effective temperature	2200 K
Stellar radius	6×10^{13} cm
Inner dust radius	4.5×10^{14} cm
Distance	1.37 kpc
Terminal velocity	15 km s^{-1}
Dust mass loss rate - superwind	1.9×10^{-6} $M_\odot$ yr^{-1}
Dust-to-gas mass ratio	3.6×10^{-3}
Gas mass loss rate - superwind	5.3×10^{-4} $M_\odot$ yr^{-1}
Gas mass loss rate - AGB wind	$\sim 10^{-6}$ $M_\odot$ yr^{-1}
Outer radius of the dust shell	10^{16} cm
CO photodissociation radius	7×10^{16} cm

4. Modelling of the circumstellar envelope of OH 26.5+0.6

Following Justtanont et al. (1996), we present a self-consistent model of the circumstellar envelope. In modelling the dusty envelope, we take into account the more recent observations by both spectrometers aboard the Infrared Space Observatory (ISO, (Kessler et al. 1996) – Short- and Long-Wavelength Spectrometers (SWS (de Graauw et al. 1996) and LWS (Clegg et al. 1996), respectively). The SWS data were taken from the archive (PI: de Jong) while the LWS data were taken from Sylvester et al. (1999). We also obtained the more sensitive 3 μm spectrum from Meyer et al. (1998) which shows an absorption due to water-ice. The model parameters are listed in Table 1. The fit to the spectral energy distribution (SED) is shown in Fig. 3. Here we use pure silicate grains as well as silicate core water-ice mantle grains. The amorphous water-ice optical constants are taken from Leger et al. (1983) as we see no sharp structures at 3 μm which signify a presence of crystalline water-ice.

Our model is able to reproduce the SED relatively well out to 200 μm (Fig. 3), considering the variability of the source as shown by photometric fluxes at different epochs. The LWS data from Sylvester et al. (1999) has the sky background subtracted. The flux level is adjusted slightly up by a factor of 1.2 to the IRAS 60 μm flux. We also adjusted the flux level of the ISO SWS spectrum so that it agrees with the IRAS 12 μm flux and the ground-based spectrum taken by CGS3 on UKIRT (Justtanont et al. 1996). The choice of the superwind radius is critical as the change of this by even 20% results in observable difference which no longer simultaneously fits the silicate 10 μm feature and the slope of the far-IR fall off. The calculated dust mass loss rate is 1.9×10^{-6} $M_\odot$ yr^{-1}.

The gas mass loss rate is calculated from the derived dust mass loss rate, assuming that the gas and dust are fully momentum coupled and that the gas outflow is driven by radiation pressure on dust grains (Goldreich & Scoville 1976; Justtanont et al. 1994). For a radiatively driven wind, the primary constraint is the observed $V_{\rm exp}$ of 15 km s^{-1} which limits the dust-to-gas mass ratio to 3.5×10^{-3}. This gives a gas mass loss rate of 5.3×10^{-4} $M_\odot$ yr^{-1} for the superwind.

Initially, a single wind with the superwind mass loss rate out to the radius of 2×10^{17} cm was used (dashed line in Fig. 4) to model the observed CO line profiles up to the first four rotational transitions. These model spectra were about an order of magnitude too bright for all the lines because the density was just too high in the outer part of the envelope. In a second model, the single wind was used again, but for this case the wind was abruptly terminated at the superwind outer radius (~0.5″, 133 R_*). These model spectra provide a fair fit to the data, but in general the intensities were about 10–25% too low.

In order to get the best fit to the observed data, a low density AGB wind is needed outside the high density superwind. Observational evidence for the presence of this tenuous outer wind is found in the OH maser and CO maps. Although the ^{12}CO $J = 1$–0 images have a low signal-to-noise ratio and the outer wind is only partially resolved, the deconvolved source emission extends out to 8.5″ × 5.5″ (*FWHM*). The observed size of the CO envelope is comparable to the CO photodissociation model by Mamon et al. (1988). OH maser maps also reveal that maser emission was seen out to 4″ in radius (Bowers & Johnston 1990). Furthermore, the presence of an AGB wind is expected since mass loss occurs during the entire AGB lifespan, well before the recent (~200 years) onset of the superwind.

For the outer portion of the envelope, past the superwind region, the derive mass loss rate is $\sim 10^{-6}$ $M_\odot$ yr^{-1}. The SED fit provides tight constraints to the superwind parameters, however the AGB dust mass loss rate is not well determined. Furthermore, for low densities, the gas and dust are not fully coupled, such that the dust flows through the envelope without interacting much with the gas. Our calculation does not account for this, so we have chosen to relax constraining the radiatively driven AGB wind to have an expansion velocity of 15 km s^{-1}. Instead we have allowed a 5 km s^{-1} margin of error to compensate for the diminished dust to gas coupling. Without the margin of error, we could not find parameters that satisfy the 15 km s^{-1} expansion velocity, while producing good fits to the line emission.

We assume no interaction exists between the two winds, i.e., there are no shocks as both winds flow at the same velocity. No observational evidence for shocks have been found. The CO and OH expansion velocities are consistent. Furthermore, ISO LWS detections of both the [O I] 63 μm and the [C II] 158 μm lines are from galactic background emission (Castro-Carrizo et al. 2001).

The calculated CO density profile is plotted in the upper panel of Fig. 4. The density profile (solid line) is a composite of the superwind and the AGB wind. The dashed line represents a single wind with the superwind mass loss rate. At 133 R_*, the density steps down from the superwind to the AGB wind. At the periphery of the envelope, the CO density falls off rapidly because of photodissociation. Simultaneously, the gas kinetic temperature structure (the bottom panel of Fig. 4) is obtained by solving for the energy balance of the gas following Goldreich & Scoville (1976) and Justtanont et al. (1994). At the superwind/AGB wind interface the temperature jumps upwards because additional heating associated with the density drop off. The lower density causes the dust-gas drift velocity to increase leading to higher heating rates. In addition, H_2O, the

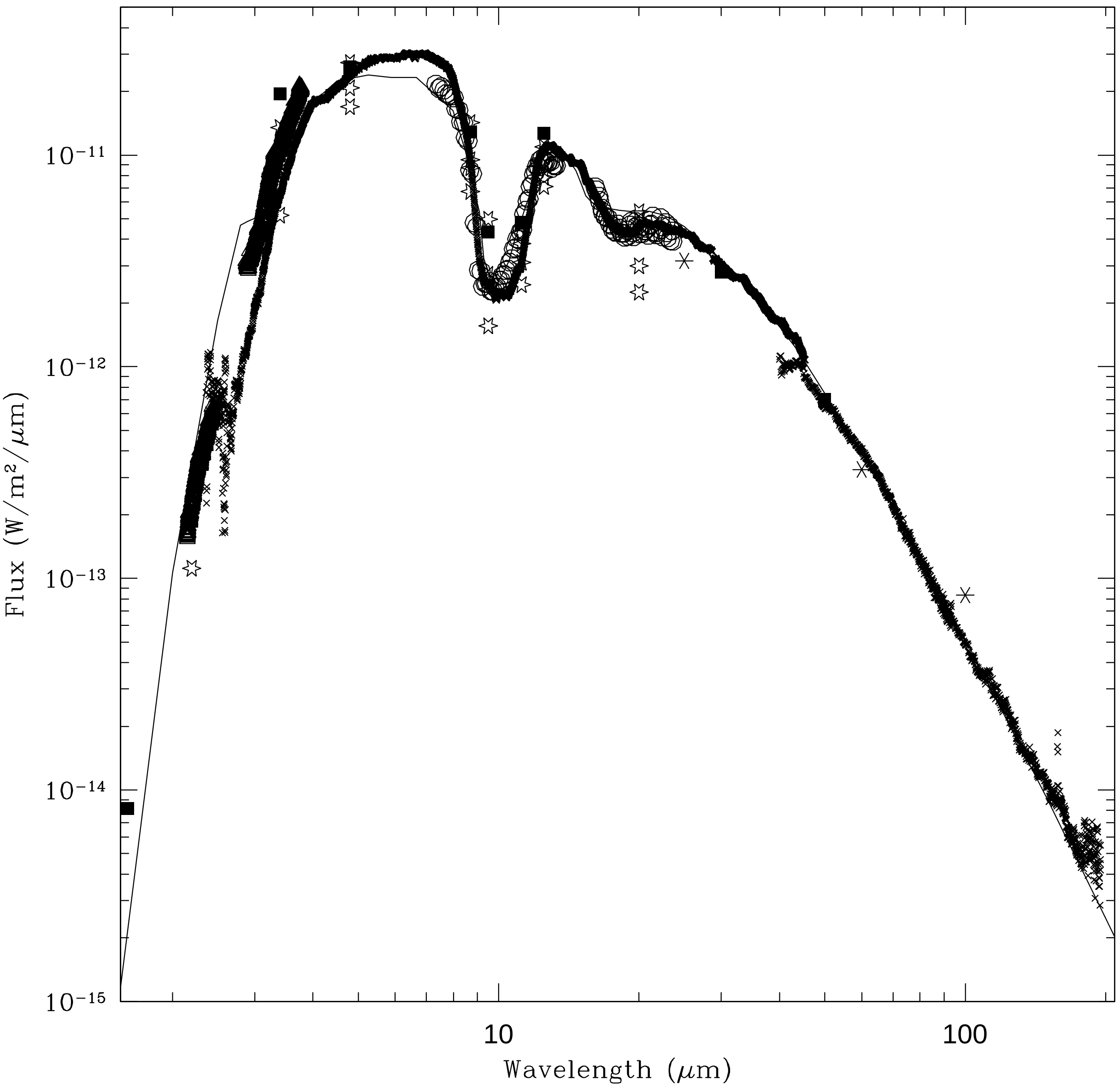

Fig. 3. A fit to the SED (solid line) using composite grains of silicate and silicate core-ice mantle. Crosses are ISO-SWS (from archive - PI. de Jong) and LWS spectra (Sylvester et al. 1999), asterisks are IRAS PSC fluxes, open circles are the UKIRT CGS3 spectrum, triangles are near-IR spectrum from Meyer et al. (1998), and filled squares and stars are photometry from Werner et al. (1980) and Evans & Beckwith (1977), respectively.

main coolant scales with the mass loss rate, thus the density and the extent of H_2O decreases in the AGB wind (Justtanont et al. 1994). The H_2O photodissociation radius was estimated from the OH maser inner radius to be about 1.5″ (Bowers & Johnston 1990). The temperature profile has slightly changed from the one used in Justtanont et al. (1996) because of the inclusion of the photoelectric heating. The temperature profile within the superwind region is unaffected, but the kinetic temperature in the AGB wind is slightly hotter.

After modelling the gas kinetic temperature and density distribution of the envelope, the CO emission can be solved through a full radiative transfer code for molecular rotational line emission developed by Schönberg (1988). The details of the current implementation are presented in Justtanont et al. (1994, 1996) and Skinner et al. (1999). Model maps of the ^{12}CO $J = 1$–0 emission are created by taking the radial intensity profile and rotating it around the origin. The model maps are then convolved by the CLEAN beam to make the final images.

5. Comparison of the model with the CO observations

The model line profiles for the CO transitions (Figs. 2 and 5) fit the observed data reasonably well, considering that the lines suffer from interstellar contamination and that the missing blue-shifted wing in the $J = 1$–0 and 2–1 lines is caused by interstellar absorption. The model spectra also slightly overestimate the brightness of the lines. Similarly, the model ^{12}CO $J = 1$–0 maps (Fig. 6) are in reasonable agreement with the

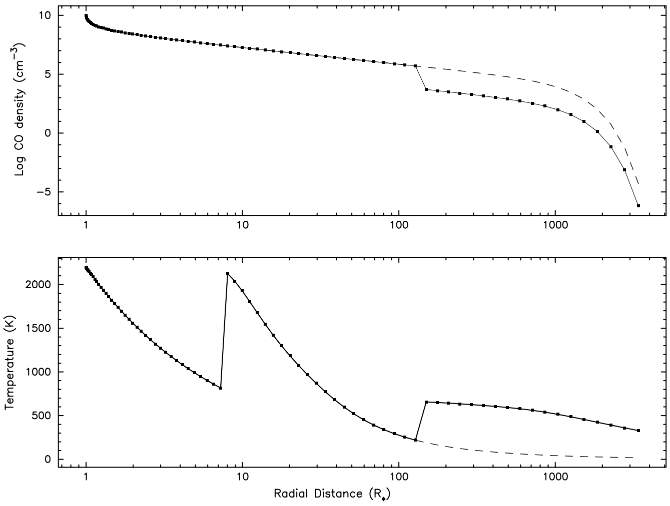

Fig. 4. The calculated density and kinetic temperature of the circumstellar envelope around OH 26.5+0.6. The dashed line represents a single wind with the superwind mass loss rate. Note the break due to the difference of the mass loss rates – superwind and AGB wind, as we assume that there is no interaction between the two.

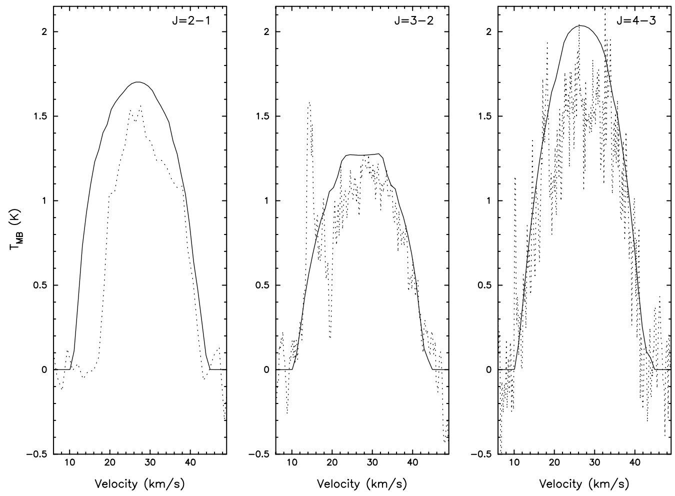

Fig. 5. Model fits of the CO rotational lines (solid) compared to the observed J = 2–1 (Heske et al. 1990), J = 3–2 and J = 4–3 (Justtanont et al. 1996) line transitions (dotted line).

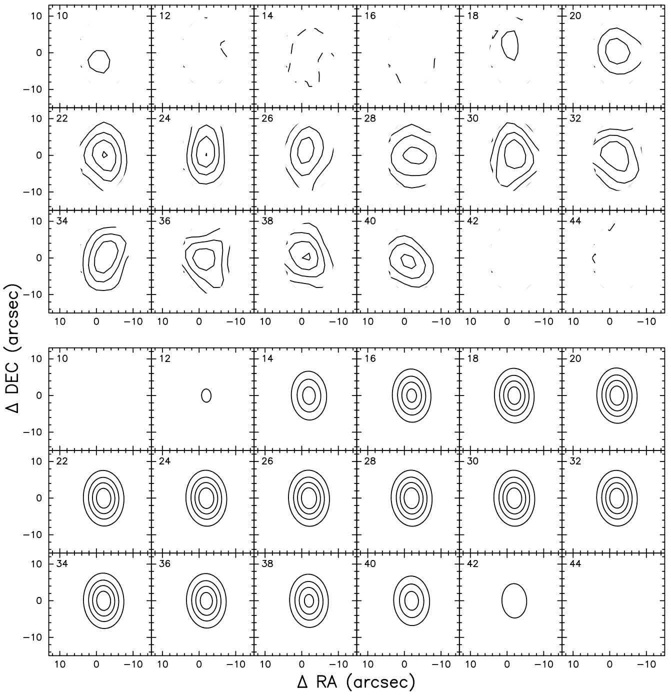

Fig. 6. The observed channel maps with the emission outside 2× the beam area masked to separate out the intervening interstellar clouds (top panels) and the model CO maps (bottom panels). Our model shows that CO emission is expected to range from 12 to 42 km s^{-1}, while the observations reveal missing flux between 12–20 km s^{-1} due to interstellar absorption.

observations, except for the deficiencies mentioned above. The spatial extent of the model images is comparable to the masked CO emission used to separate out the intervening interstellar contamination. The CO emission at 18 and 20 km s^{-1} are weaker and smaller in extent than the model maps because of the absorption. The degree of absorption can be estimated by comparing the intensities of the model and observed line profiles. The comparison shows that the absorption runs from about 12–20 km s^{-1}.

From our two-wind model, we see that the majority of the ^{12}CO J = 1–0 emission is found in the superwind and not the AGB wind. About 80% of the flux originates in the superwind and the AGB wind contributes the remaining 20% of the flux. Our model shows that the J = 1–0 emission peaks near the edge of the superwind region ($<0.5''$) where the density is $\sim10^6$ cm^{-3} and the temperature is ~300 K. Although the structure of the superwind is not resolved by the observations, its presence can be inferred from 1) the compact, $<0.5''$, mid-IR dust emitting region (Justtanont et al. 1996), 2) the deep 10 and 20 μm silicate absorption features and 3) the the fit to the IR SED.

A comparison of the radial intensity profile between the ^{12}CO J = 1–0 data and the radiative transfer model is shown in Fig. 7. The radial profiles are created by calculating the average surface brightness of an image in elliptical annuli of $0.5''$ widths. The error bars show the rms deviation due to the clumpiness of the emission. Since the velocity channels closest to the systemic velocity was contaminated by interstellar emission, an adjacent contamination free channel, 24 km s^{-1}, was plotted instead. The model CO profile reasonably agrees with the observed emission. The close correspondence between the model and beam profiles in the inner half of the envelope appears because the majority of the flux resides in the unresolved superwind region.

6. Conclusion

We present a self-consistent model of the circumstellar envelope of OH 26.5+0.6 in order to explain the BIMA observations. The envelope is detected and is partially resolved for the first time in the ^{12}CO J = 1–0 transition. With the ISO-LWS spectrum, we are able to constrain the superwind radius to 10^{16} cm from modelling the infrared dust emission. The density of the more tenuous AGB wind cannot be constrained by

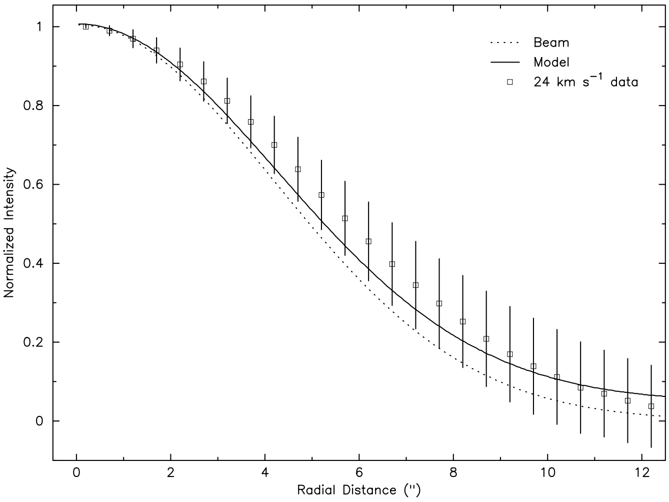

Fig. 7. The radial intensity comparison between the CO model and the observed $J = 1$–0 profile. The data points show that the envelope is partially resolved by the observations and the model prediction sufficiently traces the observed profile.

fitting the SED. We are able to fit the observed ^{12}CO $J = 1$–0 data reasonably well. We note that there appears to be missing flux between 12–20 km s^{-1} which is most likely due to the interstellar absorption along the line of sight. In order to explain the extent and intensity of the observed CO maps, we need to include a second, more tenuous AGB wind, exterior to the high density superwind. Unfortunately, the AGB mass loss cannot be well constrained by modelling the CO line since the majority of the flux originates in the unresolved superwind region. We are only able to put an upper limit of 10^{-6} $M_{\odot}$ yr^{-1} for the AGB wind. We assume there is no interaction between the superwind and the AGB wind since we find no evidence of shock excited emission.

Future observations require sub-arcsecond angular resolution at multiple rotational transitions in order to resolve the structure of the superwind and to better constrain the physical conditions of this intriguing OH/IR star at the end stages of its life on the AGB. These observations are well suited to the capabilities of infrared interferometry with the VLTI and the next generation of mm/submm interferometers, particularly the SMA and ALMA.

Acknowledgements. D. Fong and M. Meixner have been supported by NSF AST 99-81363 and the University of Illinois. Meixner has also been supported by NSF AST 97-33697. We thank our referee, R. Bachiller, for his valuable comments on our paper.

References

Bower, P. F., & Johnston, K. J. 1990, ApJ, 354, 676
Bujarrabal, V., Alcolea, J., Sánchez Contreras, C., & Sahai, R. 2002, A&A, 389, 271
Burton, W. B. 1988, Galactic and Extragalactic Radio Astronomy, ed. G. L. Verschuur, & K. I. Kellermann, 295
Castro-Carrizo, A., Bujarrabal, V., Fong, D., et al. 2001, A&A, 367, 674
Clegg, P. E., Ade, P. A. R., Armand, C., et al. 1996, A&A, 315, L38
de Graauw, Th., Haser, L., Beintema, D. A., et al. 1996, A&A, 315, L49
Evans, N. J., & Beckwith, S. 1977, ApJ, 217, 729
Goldreich, P., & Scoville, N. 1976, ApJ, 205, 144
Helfer, T. T., Vogel, S. N., Lugten, J. B., & Teuben, P. J. 2002, PASP, 114, 350
Heske, A., Forveille, T., Omont, A., van der Veen, W. E. C. J., & Habing, H. J. 1990, A&A, 239, 173
Hollenbach, D. J., & Tielens, A. G. G. M. 1997, ARA&A, 35, 179
Iben, Jr. I., & Renzini, A. 1985, ARA&A, 21, 271
Justtanont, K., Skinner, C. J., & Tielens, A. G. G. M. 1994, ApJ, 435, 852
Justtanont, K., Skinner, C. J., Tielens, A. G. G. M., Meixner, M., & Baas, F. 1996, ApJ, 456, 337
Kessler, M. F., Steinz, J. A., Anderegg, M. E., et al. 1996, A&A, 315, L27
Leger, A., Gauthier, S., Defourneau, D., & Rouan, D. 1983, A&A, 117, 164
Mamon, G. A., Glassgold, A. E., & Huggins, P. J. 1988, ApJ, 328, 797
Mauron, N., & Higgins, P. J. 1999, A&A, 349, 203
Meixner, M., Campbell, M. T., Welch, W. J., & Likkel, L. 1998, ApJ, 509, 392
Meyer, A. W., Smith, R. G., Charnley, S. B., & Pendleton, Y. J. 1998, AJ, 115, 2509
Neri, R., Kahane, C., Lucas, R., Bujarrabal, V., & Loup, C. 1998, AAS, 130, 1
Olofsson, H., Bergman, P., Lucas, R., et al. 2000, A&A, 353, 583
Sahai, R., Hines, D. C., Kastner, J. H., et al. 1998, ApJ, 492, 163
Sault, R. J., Teuben, P. J., & Wright, M. C. H. 1995, Astronomical Data Analysis Software and Systems IV, ed. R. A. Shaw, H. E. Payne, & J. J. E. Hayes, ASP Conf. Ser., 77, 433
Schönberg, K. 1988, A&A, 195, 198
Skinner, C. J., Justtanont, K., Tielens, A. G. G. M., et al. 1999, MNRAS, 302, 293
Sylvester, R. J., Kemper, F., Barlow, M. J., et al. 1999, A&A, 352, 587
te Lintel Hekkert, P., Versteege-Hensel, H. A., Habing, H. J., & Wiertz, M. 1989, A&AS, 78, 399
Ueta, T., Meixner, M., & Bobrowsky, M. 2000, ApJ, 528, 861
van Langevelde, H. J., van der Heiden, R., & van Schooneveld, C. 1990, A&A, 239, 193
Welch, W. J., Thornton, D. D., Plambeck, R. L., et al. 1996, PASP, 108, 93
Werner, M. W., Beckwith, S., Gatley, I., et al. 1980, ApJ, 239, 540